AGU PUBLICATIONS

JGR

Journal of Geophysical Research: Solid Earth

RESEARCH ARTICLE
10.1002/2015JB012085

Key Points:
- Strain and tilt constraints of faulting associated with volcanic deformation
- Strain and tilt precursors to volcanic earthquakes
- Campi Flegrei inflation and deflation monitored by strainmeters and tiltmeters

Correspondence to:
A. Amoruso,
aamoruso@unisa.it

Citation:
Amoruso, A., L. Crescentini, R. Scarpa, R. Bilham, A. T. Linde, and I. S. Sacks (2015), Abrupt magma chamber contraction and microseismicity at Campi Flegrei, Italy: Cause and effect determined from strainmeters and tiltmeters, *J. Geophys. Res. Solid Earth*, *120*, 5467–5478, doi:10.1002/2015JB012085.

Received 2 APR 2015
Accepted 20 JUL 2015
Accepted article online 24 JUL 2015
Published online 21 AUG 2015

Abrupt magma chamber contraction and microseismicity at Campi Flegrei, Italy: Cause and effect determined from strainmeters and tiltmeters

Antonella Amoruso[1], Luca Crescentini[2], Roberto Scarpa[2], Roger Bilham[3], Alan T. Linde[4], and I. Selwyn Sacks [4]

[1]Department of Chemistry and Biology, University of Salerno, Fisciano, Italy, [2]Department of Physics, University of Salerno, Fisciano, Italy, [3]CIRES & Department of Geological Sciences, University of Colorado at Boulder, Colorado, USA, [4]Department of Terrestrial Magnetism, Carnegie Institution of Washington, Washington, District of Columbia, USA

Abstract In March 2010 two borehole strainmeters and three Michelson tiltmeters within the Campi Flegrei volcanic system, Italy, registered an abrupt deformation signal that was followed 20 min later by seismic slip on a pair of onshore normal faults. We demonstrate that the observed strain changes were caused by a small but rapid volume decrease in a previously identified offshore ellipsoidal magma source or part of it. Although the total deflation was below the detectability of interferometric synthetic aperture radar and GPS, deflation observed rates were briefly 2 orders of magnitude more rapid than decadal inflation rates. We conclude that this high dilatational contraction rate was responsible for triggering seismicity and that this process may be responsible for the normal faulting often observed in the Campi Flegrei region. Our study quantifies the crucial role played by a transient, minor reduction in dilatational stress, in triggering slip on a fault near critical failure. Our subsurface measurements of strain and tilt registered anomalous deformation three sigma above background noise levels 17 min before the onset of microseismicity suggesting strain measurements have potential utility as an early warning system for the city of Naples.

1. Introduction

Earthquakes associated with the movement of magma near volcanoes are generically known as volcano-tectonic earthquakes (VT). In addition to volumetric and thermal stresses from magma intrusion and transfer, such earthquakes are known to be influenced by regional stress, gravitational loading, variations in pore pressure, and by hydraulic fracturing. The frequent triggering of VT events from the passage of seismic waves from distant earthquakes [*McNutt*, 2005] suggests that stress conditions in VT regions are close to critical failure. *Toda et al.* [2002] have shown that any sustained increase in stressing rate (whether due to an intrusion, extrusion, or creep event) may control the seismicity rate, in accord with a laboratory-based rate/state constitutive law.

Here we take advantage of a unique set of tiltmeter, strainmeter, and microseismicity data to investigate the links between small but rapid surface deformation and faulting. In particular, we analyze an abrupt 40 min change in strain and tilt recorded on 30 March 2010 at Campi Flegrei (CF) caldera, Italy, by subsurface strainmeters and tiltmeters, that was accompanied 20 min into the event by a swarm of microearthquakes. The earthquakes appear to have been initiated at maximum peak strain rates.

Although the total deflation was below the detectability of interferometric synthetic aperture radar (InSAR) and GPS, deflation-observed rates were briefly 2 orders of magnitude more rapid than decadal inflation rates. Our study reveals the critical role played by transient stress-rates in inducing fault slip and suggests that transient strain changes may have utility in forecasting the onset of future damaging seismicity.

2. Study Area Setting

The Campi Flegrei (CF) caldera, Italy, is located within a densely populated volcanic region in the western suburbs of Naples (population 3 million). The coast near Campi Flegrei is renowned for its volcanically related vertical ground motions that have submerged a Roman market relative to sea level and whose subsequent

partial emergence is recorded by elevated populations of Lithophaga (marine molluscs) burrows and shells on the ancient columns [e.g., *Morhange et al.*, 2006]. After the eruption of Monte Nuovo in 1538, the caldera subsided and continued to do with minor reversals until 1969 when a period of uplift commenced. In the early 1970s this uplift became significant (≈1.5 m max). A further large uplift episode occurred from 1982 to 1984 (≈1.8 m max), with subsequent partial recovery (about 60 cm in 2 years). Superposed on the 20 year long subsidence, smaller uplift episodes occurred in 1989, 1994, 2000, and 2006 [e.g., *Gaeta et al.*, 2003; *Amoruso et al.*, 2007]. From 2006 to spring 2013, the Campi Flegrei region was mostly uplifting at a slow but increasing rate. Uplift restarted in spring 2014.

De Natale et al. [1995] have obtained accurate determinations of fault plane solutions (FPS) during an intense swarm-like activity in the last period of the major 1982–1984 unrest, using the joint information carried by the *P* polarity and *S* wave vector direction data sets. All the retrieved mechanisms indicate normal faulting. Among more recent papers, *D'Auria et al.* [2014] reports a more complete FPS catalog for 1982–1984, where normal mechanisms (47%) prevail on inverse and strike-slip mechanisms (23% and 30%, respectively); however, solutions are determined from first motions only and are consequently less robust.

Since 2000 slow inflation has been accompanied by infrequent small earthquakes with maximum magnitude 2.2 (see Figure 1a). *Saccorotti et al.* [2007] have studied swarms of microearthquakes that occurred in 2005–2006. Hypocenters were mainly located beneath Solfatara at depths ranging between 0.5 and 4 km; again, FPS indicate predominantly normal mechanisms.

Because the deformation pattern was confined to a relatively modest surface area (around 5 km in diameter) initial studies of the 1982–1984 uplift episode concluded that surface deformation was attributable to inflation of a quite shallow magma source (<3 km) [e.g., *Berrino et al.*, 1984]. Since no large magma chamber was detectable in seismic tomography and a small chamber would imply unacceptable high overpressure, *De Natale et al.* [1997] suggested the existence of a 4.5 km deep magma chamber whose inflation caused a deformation pattern limited by free-slipping inward-dipping ring faults. However, *Folch and Gottsmann* [2006] showed that free-slipping ring faults generate strong differences in the deformation patterns inside and outside the faults, while interferometric synthetic aperture radar (InSAR) data do not give any evidence of such differences [e.g., *Manconi et al.*, 2010; *Amoruso et al.*, 2014a; *Trasatti et al.*, 2015]. Several later studies ascribed CF unrests to fluid injections at the base of the hydrothermal system [e.g., *Battaglia et al.*, 2006; *Todesco et al.*, 2010; *Troiano et al.*, 2011].

Although there is no general consensus about the source (hydrothermal or magmatic) of CF deformation, *Amoruso et al.* [2008] showed that a pressurized penny-shaped source, about 3100 m deep and having a radius of about 2700 m, can explain ground deformation for the 1982–1984 period. Three-dimensional delay time tomography indicates the presence of a densely fractured, gas- and/or brine-bearing rock layer between 3000 m and 4000 m in depth [*Zollo et al.*, 2008]. Seismic attenuation imaging has been interpreted to signify a possible small melt volume ≈3500 m deep [*De Siena et al.*, 2010].

Using leveling data from 1980 to 1994, geodetic precise-traversing data for June 1980 and June 1983, ERS/ENVISAT SAR data from 1993 to 2010, and cGPS data from 2000 to 2013, *Amoruso et al.* [2014a, 2014b] have recently shown that surface deformation from 1980 to 2013 can be decomposed into two stationary parts. Large-scale deformation can be explained by a quasihorizontal source, oriented NW/SE and mathematically represented by a pressurized finite triaxial ellipsoid (PTE) ≈4 km deep (Figure 1), possibly related to the injection of magma and/or magmatic fluids from a deeper magma chamber into a sill, or a series of interconnected pores or cavities. From a mathematical point of view, source finiteness is accounted for using an approach similar to the multipole expansion of the gravitational potential outside a mass distribution. The dipole term is null because of symmetry, but quadrupole terms remain [*Amoruso and Crescentini*, 2011]. Residual deformation not accounted for by an inflating ellipsoidal source can be mathematically explained by a small (point) pressurized oblate spheroid (PS) ≈2 km below the Solfatara fumarolic field (Figure 1a). We interpret this second source as the poroelastic response of the substratum to pore pressure increases near the injection point of hot magmatic fluids into the hydrothermal system [*Fournier and Chardot*, 2012].

The location and geometry of the PTE and PS sources are constant over the period 1980–2013 with the exception of volume changes (potency). Potency time histories are somewhat similar but not identical.

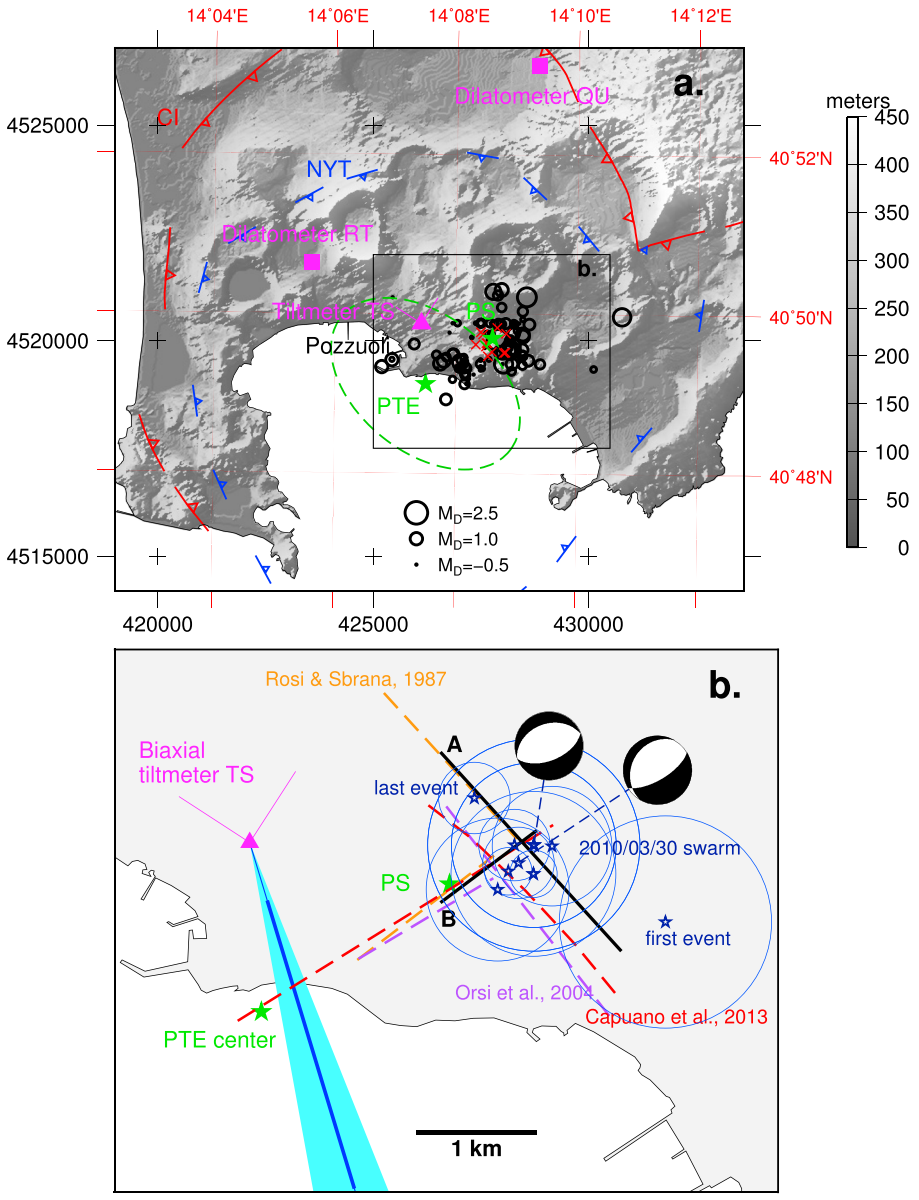

Figure 1. Map of the Campi Flegrei region showing dilatometers and tiltmeters (axes indicated); PS and PTE are subsurface inflation/deflation sources from *Amoruso et al.* [2014b]. (a) Green ellipse, PTE spatial extent; CI, Campanian Ignimbrite (39 ka) caldera; and NYT, Neapolitan Yellow Tuff (15 ka) caldera [*Orsi et al.*, 2004]. Black circles indicate seismic events from 2000 to the present (http://sismolab.ov.ingv.it/): the map only shows events whose solution quality of the hypocenters are rated A or B [*Lee and Lahr*, 1975], duration magnitudes range −1.0 to 2.2, and circles are sized according to magnitudes (see scale). Red crosses indicate main Solfatara fumaroles. (b) Blue solid line indicates the azimuth of recorded tilt, the thicker part indicating the vertical plane used in Figure 5, and cyan region indicates ±20% range. Blue stars indicate well-located microearthquakes (13 events having standard error of the epicenter, ERH, < 1 km and standard error of the focal depth, ERZ, < 1 km; 4 events share the same epicenter as others) occurred on 30 March 2010; blue circles indicate ERH; and the focal mechanisms derived for two of the events are connected to their epicenters through blue dashed lines. A and B (black solid lines) indicate faults inferred to have slipped in the earthquake swarm, and red, orange, and violet dashed lines indicate known faults mapped by various authors. [*Capuano et al.*, 2013; *Rosi and Sbrana*, 1987; *Orsi et al.*, 2004].

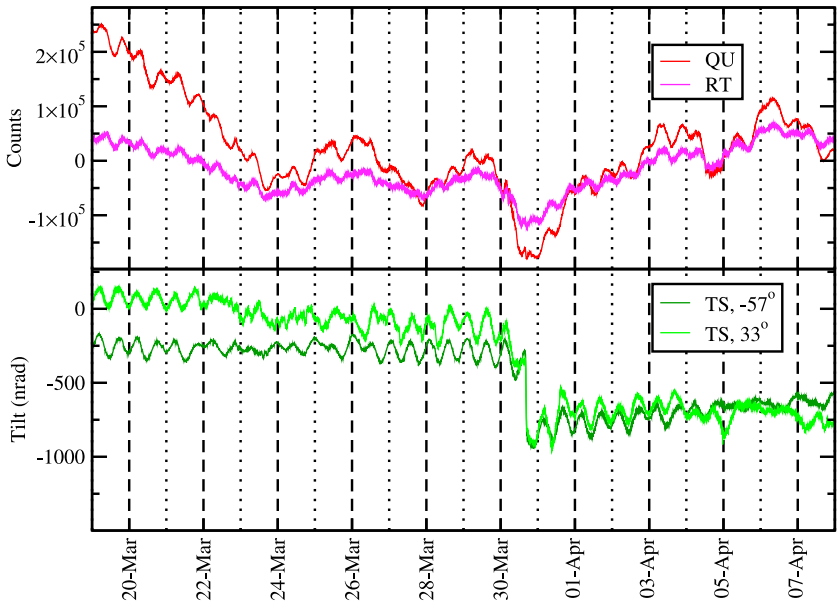

Figure 2. Deformation data plots. Dilatometer data are positive for compression, and tiltmeters data are positive for uplift toward the given azimuthal (E of N) direction.

3. Data

We use 1 min data samples from two Sacks-Evertson dilatometers (RT and QT in Figure 1) and three Michelson tiltmeters (located at TS in Figure 1). The tiltmeters are installed in tunnels at 20 m depth with azimuths of N57W (two 66 m long instruments) and N33E (28 m long). Twenty days of raw data are shown in Figure 2.

The calibration of borehole strainmeters, and to a lesser degree long base-line tiltmeters, depends on both elastic coupling between the instrument and the rock and the local rheology near the borehole. The calibration also accounts (in part at least) for the effects of horizontal heterogeneities such as the presence of caldera boundary faults or the different elastic properties of the caldera infill respect to extracaldera rocks on the strain signal. We used earth tides for strainmeters absolute calibration and teleseismic waves for additional, more accurate, strainmeters relative calibration. The dilatometer data have been analyzed for tidal and barometric response, using the approach described in *Amoruso et al.* [2000]. Results agree with those obtained within 2% using VAV code [*Venedikov et al.*, 2005]. The computation of theoretical tides included ocean loading, computed using SPOTL code [*Agnew*, 2013], TPXO8-atlas ocean model (1/30° resolution; http://volkov.oce.orst.edu/tides/tpxo8atlas.html) and a detailed coastline with ≈30 m resolution. Sea tidal predictions from TPXO8-atlas have been confirmed by comparison with measurements at Pozzuoli harbor.

In what follows, compressions are expressed as dimensionless strain, $-\Delta V/V$, where V is the instrument-sensing volume. We use the symbol nε, nanostrain, for $\Delta V/V = 10^{-9}$. Calculated observed-to-model tidal amplitude ratios for dilatational strain are 946 (284) counts/nε and 1039 (322) counts/nε for O1 and M2, respectively, for QU (RT). This indicates that the ratio between QU and RT calibration factors is about 3.3. Using surface waves recorded on 27 February 2010, the ratio between QU and RT calibration factors would be about 4. In our opinion, the relative sensitivities of the two sites is better constrained by the comparison of surface wave amplitudes; thus, we adopt (somewhat arbitrarily) a ratio of 3.8 (+0.2/−0.5) in our analysis. Taking account of the different observed-to-model tidal amplitude ratio for O1 and M2 and the uncertainties in the ocean loading computations, we assign a 20% uncertainty to QU absolute calibration (1000±200 counts/nε).

The tiltmeters data are less affected by local elastic conditions and subsurface geometry because they are long (66 m) compared to the width of the underground tunnels in which they are installed and thus are not perturbed by strain/tilt coupling. Two of the tiltmeters are identical in length and azimuth, and since the data from one are coherent with the other we use only the lower noise level instrument. In our subsequent discussion we use data from all six sensors to examine detection thresholds. The tilt data were analyzed to check their consistency with synthetic tides and to evaluate any possible tilt direction deviation due to local structure. For tilt, calculated observed-to-model tidal amplitude ratios are about 0.9 and 1.3 for O1 and M2, respectively.

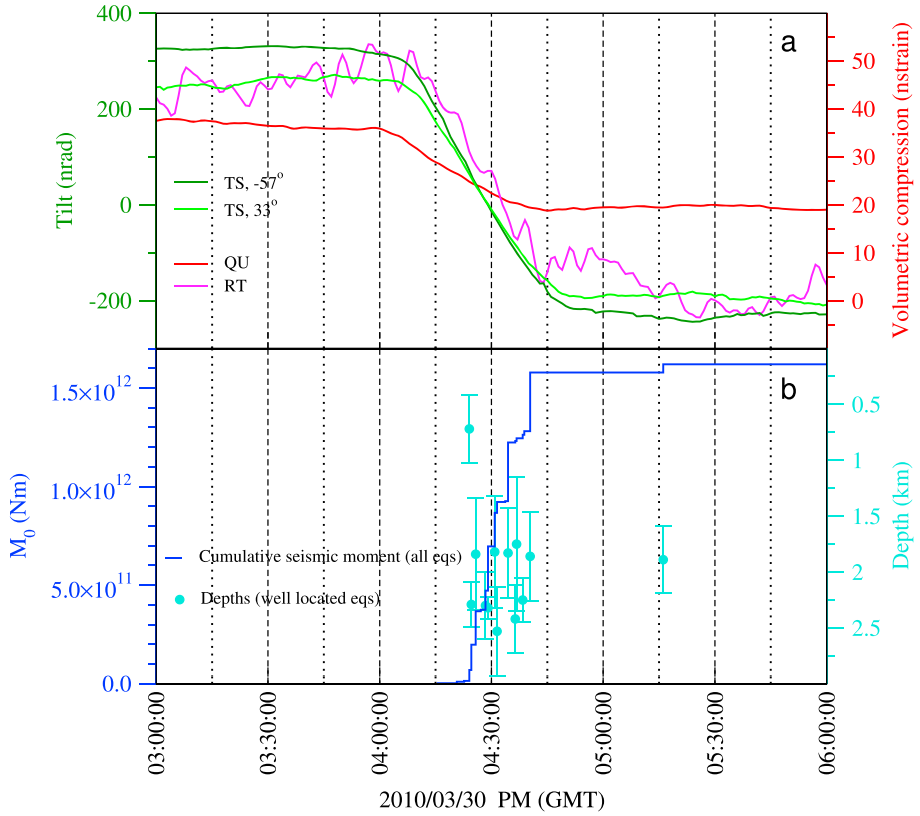

Figure 3. Deformation and seismic data. (a) Magenta and red lines indicate dilatometer data with barometric pressure and tides removed, and light and dark green lines indicate tiltmeters data with tides removed. (b) Cyan circles indicate depth of well-located microearthquakes (ERH < 1 km and ERZ < 1 km), error bars give standard errors, and solid blue line indicates cumulative seismic moment (all events).

The good agreement between predictions and observations indicates that the tidal model calculations are accurate at the 20% level and that distortion due to local structure is at most at the same 20% level.

Plots in Figure 3 show dilatometer data with barometric pressure and tides removed and tiltmeters data with tides removed. Depths of well-located microearthquakes (±1 km) occurring on 30 March 2010, and cumulative seismic moment (all events) are also shown. All the deformation signals for the 30 March 2010 event start at the same time and have approximately the same time history consistent with deformation from a single source. Signal duration is about 40 min. Estimated signal amplitudes are (i) N57W tilt, 520 nrad down to SE; (ii) N33E tilt, 440 nrad down to SW; (iii) QU dilatometer, 17 nε expansion; and (iv) RT dilatometer, 44 nε expansion. Related uncertainties are assumed to be 20% (see above).

The seismic swarm occurred on two intersecting, approximately perpendicular faults (see Figure 1b) and consisted of 19 recorded events, with duration magnitudes M_D in the range −0.5 to 1.2 (http://sismolab.ov.ingv.it/). Duration magnitude is routinely calculated by using the relation

$$M_D = -2.46 + 2.82 \log \tau \tag{1}$$

where τ is the earthquake duration, measured from the *P* wave arrival to the point at which the coda of the signal drops down the noise amplitude [*Petrosino et al.*, 2008].

The time history of the cumulative seismic moment (Nm) in Figure 3 has been obtained using the relation [*Petrosino et al.*, 2008]

$$\log M_0 = 1.22\, M_l + 9.241 = 1.22\, M_D + 10.01 \tag{2}$$

and duration magnitudes from http://sismolab.ov.ingv.it; M_l is local magnitude.

Table 1. Campi Flegrei Multilayered Elastic Models Used in This Work

Depth (km)	Vp (km/s)	Vs (Drained) (km/s)	Vs (Undrained) (km/s)	Density (kg/m^3)
0.00	1.60	0.92	0.85	1800
0.62	2.50	1.44	1.35	2100
1.40	3.20	1.85	1.78	2270
1.55	3.90	2.25	2.17	2380
2.73	3.95	2.28	2.32	2400
3.92	5.20	3.00	3.25	2580
≥4.03	5.92	3.42	3.42	2700

The solution quality of the hypocenters [*Lee and Lahr*, 1975] is C for 12 events and B for 7 events.

The swarm began about 15 to 20 min after initiation of the deformation signal near the time of maximum strain rates. Earthquakes were very small, and focal mechanism solutions could be obtained only for two of them (M. La Rocca, private communication, 2014). Both exhibited normal faulting with strike about N60E; dip was about 67° and 55° for the shallower and deeper event, respectively (see Figure 1b). We have computed deformation at TS, QU, and RT caused by a normal faulting earthquake occurring in the epicentral region of most of the microearthquakes in the swarm at 2.5 km depth, $M_0 = 2.8 \times 10^{11}$ Nm. Exact numbers depend on strike and dip angles, but tilt at TS is always of the order of 0.1 nrad, and volumetric strain at QU and RT is always of the order of 10^{-2} nε, i.e., too small to be detectable. This proves that no portion of the observed strain signal is ascribable to the microearthquakes.

4. Deformation Modeling

In what follows, we use a layered elastic medium whose parameters are constrained by local *P* wave tomography [*Amoruso et al.*, 2007, 2008, 2014a, 2014b].

Elastic parameters of the layered half-space are obtained from the 1-D Vp model in the work by *Judenherc and Zollo* [2004] and the Nafe-Drake curve [*Ludwig et al.*, 1970] taking into account the drained response of the medium by setting the Poisson's ratio to 0.25 at all depths. Even if the Nafe-Drake curve may be inappropriate to an explosive volcanic environment like CF, nevertheless, we obtain a density profile very similar to the one inferred by the Italian Oil Agency from gravity anomalies (2000 kg/m^3, above 1 km depth; 2200 kg/m^3, 1 to 2.4 km; 2400 kg/m^3, 2.4 to 3.2 km; 2600 kg/m^3 below 3.2 km depth) [*AGIP*, 1987]. Values for intermediate depths are obtained by linear interpolation between adjacent listed depths. We have also tested the undrained response of the medium by using 1-D *S* wave velocities from the 3-D Vp/Vs model in *Chiarabba et al.* [2006]; results obtained in the undrained case are very similar to those obtained in the drained case and are not shown here for brevity. The drained and undrained models are summarized in Table 1.

4.1. Qualitative Constraints on Source Location

The fact that we have observations of this deformation transient at only three locations makes it impossible to constrain the source uniquely. For example, if a slow earthquake was assumed, trade offs among fault location, geometry, and focal mechanism would permit a source almost anywhere within the CF area. However, it is evident that observations (i) are consistent with expansion of our hypothesized PTE source and (ii) delimit unambiguously the 3-D volume (spheroidal source permitted region, SSPR in Figure 4) where a very small spheroidal expansive source capable of accounting for the observations themselves must be located. In other words, both a deflation of the entire PTE or a part of it satisfies the observations.

For a spherical point pressure source surface tilt will point down toward a deflating source or up away from an inflating source. The tilt vector at TS (about 680 nrad in magnitude) points down toward the south and passes close to the location of the PTE source center (see Figure 1b). Deflation of the PTE source also results in expansion at the two strainmeters sites, as is observed. An inflating source to the north of the tiltmeters could also induce tilt down to the south but would result in contraction at the dilatometers, contrary to what is observed.

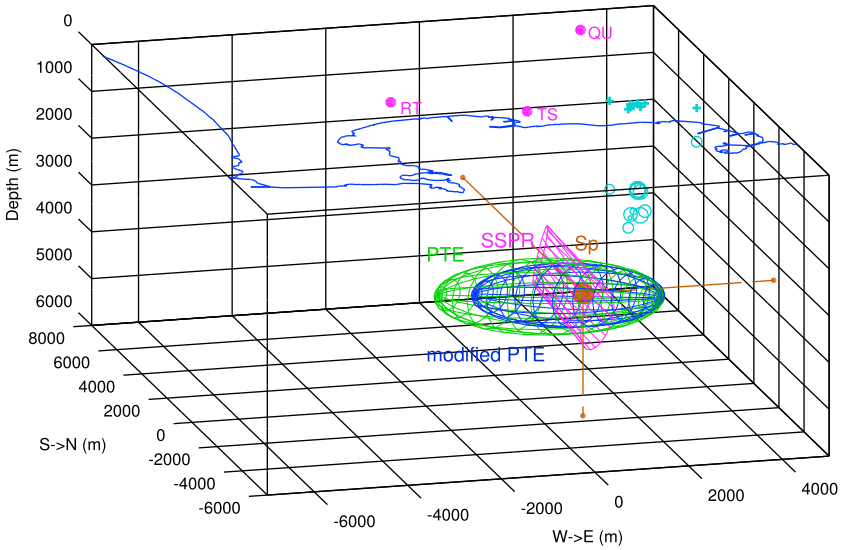

Figure 4. The 3-D sketch of station locations (magenta-filled circles), well-located (ERH < 1 km and ERZ < 1 km) earthquake hypocenters (cyan circles) and epicenters (cyan pluses), PTE (green wired ellipsoid), modified PTE (blue wired ellipsoid), SSPR (magenta wired flat frustum), and Sp (maroon sphere). Dashed maroon lines give the Sp orthogonal projection onto the gridded reference planes. Horizontal coordinate origin is at UTM WGS84 33T 425819 m E 4519866 m N.

4.2. Quantitative Approach

From the above logic we note that deflation of the hypothesized PTE source (green ellipsoid in Figure 4) is consistent with the data. A volume change of -4.5×10^4 m^3 (computed as in *Amoruso and Crescentini* [2009]) of a modified PTE (blue ellipsoid in Figure 4) gives (i) N57W, 530 nrad tilt down to SE; (ii) N33E, 445 nrad tilt down to SW; (iii) QU dilatometer, 18 nε, dilatation; and (iv) RT dilatometer, 43 nε, dilatation, close to what we observe.

We have also tested alternative expansive source geometries that may account for the strain observations. In our search for acceptable solutions the tilt vector and its uncertainty at TS defines the azimuthal location of the source (thick blue line in Figure 1b), and the distance to the source is determined by the ratio of amplitudes

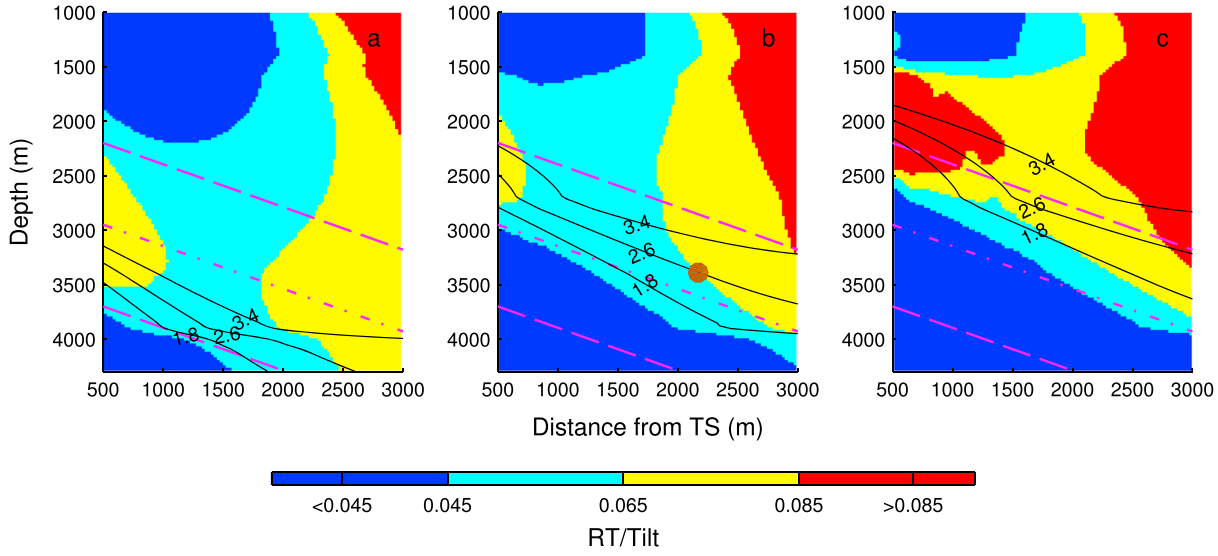

Figure 5. RT/Tilt (nε/nrad, color map) and RT/QU (contour lines) for a small (point) expansive spheroidal source located on a vertical plane (thick blue line in Figure 1b) oriented as the observed tilt azimuth. Acceptable RT/QU ranges 1.8 to 3.4; acceptable RT/Tilt ranges 0.045 to 0.085. (a) Oblate spheroid, (b) sphere, and (c) prolate spheroid. Dashed magenta lines indicate intersection with SSPR (see Figure 4), and dash-dotted magenta lines indicate SSPR axis. Filled maroon circle indicate location of the small spherical source (Sp) which satisfies data exactly and is used for computing Coulomb stress changes.

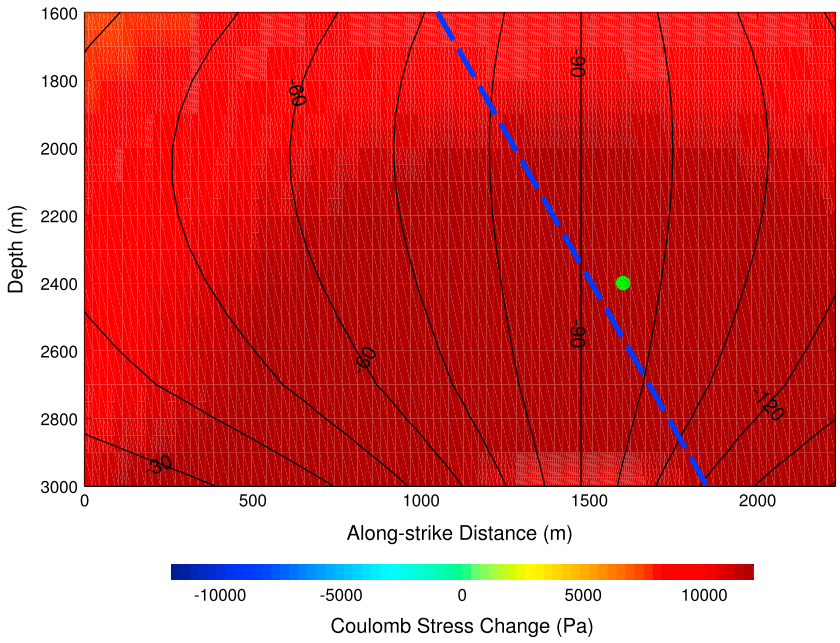

Figure 6. Color map of Coulomb stress changes on fault A due to deflation of the spherical source Sp (Figure4). Contours show the direction (counterclockwise relative to strike) of the traction vector component parallel to the fault, i. e., the expected rake angle in case of triggered fault slip. Dashed blue line indicates intersection between fault A and fault B, and green circle indicates normal faulting earthquake on fault A used to compute Coulomb stress changes on fault B. Frictional coefficient is 0.5, and B is 0.9, because of the high level of water saturation at CF.

recorded by the strainmeters and tiltmeters (RT/tilt, RT/QU, etc.). We calculated the ratios between volumetric strain and tilts for deflating point sources (oblate spheroids, aspect ratio 0.5; spheres; and prolate spheroids, aspect ratio 2) located on a vertical plane at that orientation (VP in what follows). Volumetric strain and tilts (through the relative vertical displacements of the tiltmeters ends) were computed as in *Amoruso et al.* [2014a] (Appendix A). Results are shown in Figure 5.

Taking into account data uncertainties, an acceptable RT/QU amplitude ratio is 2.6 ± 0.8, and an acceptable RT/Tilt ratio is 0.065 ± 0.020. These ranges define the above mentioned SSPR, which includes part of our hypothesized PTE source. We schematize SSPR as a solid figure resembling a right elliptic cylinder (Figure 4). Its axis lies on VP (dash-dotted magenta line in Figure 5); the minor axis of its elliptical section is perpendicular to VP and has a length which increases with distance from TS, to account for the uncertainty in the observed tilt direction at TS; the major axis of its elliptical section lies on VP and has constant length.

For computational simplicity, we next adopt a small sphere inside SSPR (Sp in Figure 4; maroon-filled circle in Figure 5b) as the source to investigate whether the strain changes accompanying its deflation are consistent with the mechanism and locations of subsequent earthquakes. Sp satisfies the observations exactly when its potency (volume change) is 6.75×10^4 m^3; computed maximum ground displacement is about 2.5 (1.2) mm for the vertical (horizontal) component.

5. Deflation-Induced Stress on Seismically Activated Faults

Most of the best-located triggered microearthquakes occurred close to the intersection of two previously mapped approximately orthogonal faults (see Figure 1b). Since the two faults are mapped with subtle differences by different authors, we have schematized their locations and lengths using the solid black lines in Figure 1b and refer to them as faults A and B. Fault A strikes ≈N138E; fault B strikes ≈N54E. The two events for which focal mechanisms were obtained are both normal faulting (see Figure 1b) with strike about N60E consistent with fault B geometry; dip was about 67° for the shallower event and 55° for the deeper event (M. La Rocca, private communication, 2014). We simplify fault B to be vertical at depths shallower than 1500 m and to dip at 60° below 1500 m to match the mapped fault trace. For fault A we have no information, but most authors assume it to be nearly vertical [e. g., *Orsi et al.*, 2004]; thus, we assign a dip of 85° for fault A. Intriguingly, fault B lies between PTE and PS and thus might represent a preferential path for magmatic fluids.

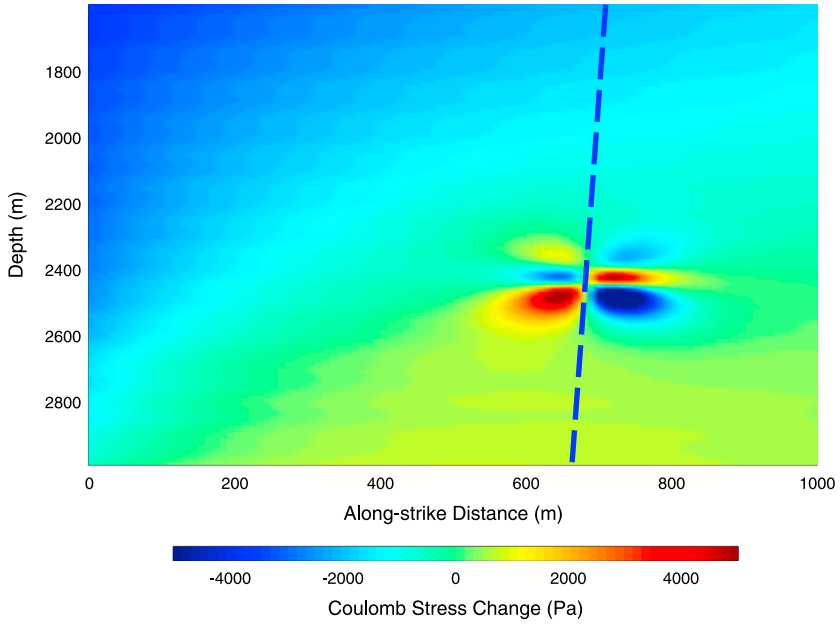

Figure 7. Color map of Coulomb stress changes on fault B due to both Sp (Figure 4) and a normal faulting earthquake (M_l=1.2) occurring on fault A, close to the intersection between the two faults (Figure 6). Dashed blue line indicates intersection between fault B and fault A. Frictional coefficient is 0.5, and B is 0.9, because of the high level of water saturation at CF.

Generally speaking, high-permeability fault gouges might favor gas leakage from the PTE and consequent depressurization of the entire sill or part of it.

We have computed Coulomb stress change $\Delta\sigma_C$ on faults A and B, due to Sp. Following *Harris* [1998], we use the expression

$$\Delta\sigma_C = \Delta\sigma_S + \mu\,(1 - B)\,\Delta\sigma_N \tag{3}$$

where $\Delta\sigma_S$ is the change in shear stress, $\Delta\sigma_N$ is the change in normal stress (positive for extension), μ is the frictional coefficient, and B is a coefficient similar to the Skempton coefficient. equation (3) holds for the undrained situation immediately after the static stress changes have occurred but before fluids have had a chance to flow freely; the fault zone materials are assumed to be more ductile than the surrounding materials [*Harris*, 1998]. In detail, we have schematized the source through suitable moment tensors [*Amoruso et al.*, 2014a, Appendix A] and computed (i) the components σ_{ij} of the stress tensor over the fault using PSGRN/PSCMP code version 4.4 [*Wang et al.*, 2006]; (ii) the components T_j of the traction vector through the Cauchy's formula $T_j = \sum_i \sigma_{ij} n_i$, n_i being the components of the unit normal on the fault; and (iii) shear and normal stress as $\sigma_N = \sum_i T_i n_i$ and $\sigma_S = \sqrt{T^2 - \sigma_N^2}$.

Results for fault A are shown in Figure 6. Deflation-induced stress favors normal faulting earthquakes, because of the large positive Coulomb stress change and the direction of the traction component parallel to the fault. Reasonable changes of the source location (hundreds of meters) do not affect this result except in minor details. In contrast, Coulomb stress change on fault B (not shown for brevity) is negligible and appears insufficient to trigger earthquakes. A possible mechanism for triggering earthquakes on both faults is that (i) source deflation initially triggered normal faulting on fault A; subsequently, (ii) slip of fault A triggered normal faulting events on fault B.

To test this hypothesis, we also take account of the regional stress field. For the past 0.7 Ma, tectonic movements have favored the relative SE displacement of the Tyrhennian side of Italy, which has in part been accommodated by ESE-WNW extensions [*Milia et al.*, 2009]. This regional stress has little influence on fault A but favors normal slip on fault B. Because of this realistic assumption, the first term in equation (3) becomes $\Delta\sigma_{\mathrm{dip}}$, which is the change in shear stress in the along-dip direction [*Harris*, 1998]. We have computed $\Delta\sigma_{\mathrm{dip}}$ from deflation of source Sp and a normal faulting earthquake (M_l = 1.2) occurring on fault A, close to the intersection between the two faults (green circle in Figure 6). Near the intersection of the two faults, $\Delta\sigma_C$

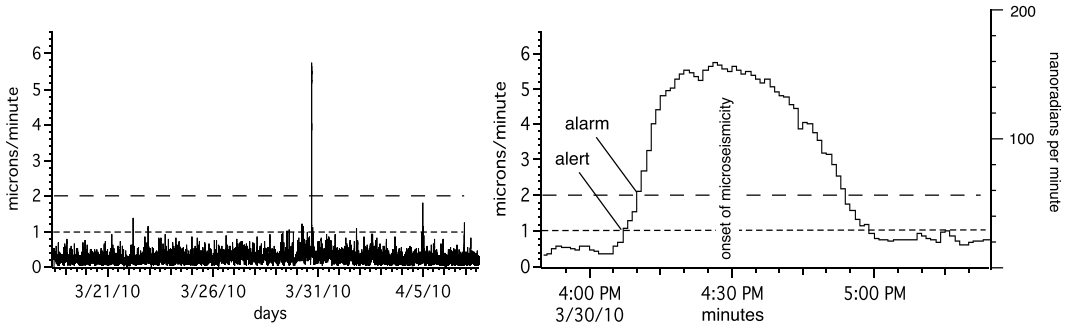

Figure 8. tiltmeters data: modulus of the difference of the instantaneous value for water level change from its average value for the preceding 10 min, averaged for all six sensors. The 2010 tilt signal is a factor of 6 above the background noise level (RMS ≈0.3μm/min) in the month of raw data illustrated. Detection thresholds of 1 and 2 μm/min (30 and 60 nrad/min) are exceeded 3 min and 6 min, respectively, after the start of deflation.

on fault B reaches values as large as thousands of Pa, supporting the hypothesized triggering process (see Figure 7). Far from the intersection between fault A and fault B no microearthquakes occurred on fault B (see Figure 1), consistent with the small computed values of $\Delta\sigma_C$.

6. Discussion

Our calculations suggest that static stress changes associated with a rapidly deflating shallow magma source triggered a swarm of normal faulting earthquakes approximately 3 km to its NE. The swarm started when strain changes, and presumably stress changes, attained about half their maximum value (Figure 3) and when strain rate changes attained their maximum value (Figure 8). The delay of tens of minutes between strain changes and the onset of microseismicity suggests either that the normal fault system where the microseismic swarm occurred was close to failure, but not precisely at a critical state prior to deflation, or that poroelasticity may have played a role in moderating the failure process. Alternatively, the coincidence between maximum strain rates and microseismicity may signify that a threshold strain rate may be a critical condition for inducing seismicity.

Although long-term deformation results in much larger cumulative stresses, our study suggests that transient stress rate plays a critical role in inducing fault slip. For example, during the 2011–2013 uplift, the mean volume change rate in our hypothesized ellipsoidal source was about 200 m^3/h [*Amoruso et al.*, 2014b], compared to the volume decrease of ≈100,000 m^3/h during the recorded March 2010 deformation event. That is, the deflation rates that caused seismicity exceeded long term inflation rates by a factor of 500. We are uncertain whether our observation applies in general to swarm activity in the Campi Flegrei region because our observations describe what might be an unique event. A significant seismic swarm occurred on 7 September 2012, [e. g., *Amoruso et al.*, 2014b], but unfortunately, tiltmeters or dilatometer data were unavailable at this time (only RT was operating). Nor are data recorded both by strainmeters and tiltmeters available from times of other seismic swarms in the region.

The observation that deflation precedes seismicity by tens of minutes may be of utility in forecasting the onset of future damaging seismicity. Because of their <2 km proximity to the deflating PTE source, the tiltmeters are of particular interest since their signal-to-noise ratio at the 1 min sampling interval for each sensor is a factor of 4–10 even without the removal of harbor seiche loading, temperature effects, and tides. The 40 min deflation episode we have discussed corresponds to a 1.8 mm change of water level at each end of the 66 m long tiltmeters and 0.6 mm change in the 28 m long tiltmeters, transient deformation that is without precedent during the time we have been recording.

Assuming that strain rate or tilt rate is crucial, as discussed above, we examined various time derivatives of the data. In Figure 8 we plot the modulus of the difference of the instantaneous value for water level change from its average value for the preceding 10 min, averaged for all six sensors:

$$\bar{y} = \frac{\sum_{i=1}^{6} \Delta y_i}{6} = \frac{\sum_{i=1}^{6} \left| y_i(t) - \sum_{j=1}^{10} y_i(t-j)/10 \right|}{6} \quad (4)$$

where *i* is the sensor index. Since all six sensors are independent, stacking the data suppresses thermal and electronic sensor noise by a factor of 2.5 resulting in an RMS rate noise of roughly 10 nrad/min. Using the above algorithm, an automatic alert could have been issued after 3 min when tilt rates exceeded normal background noise levels of 30 nrad/min, and an unique alarm would have been possible after 6 min when the signal exceeded 60 nrad/min, the largest peak signal recorded elsewhere in the data. Using this algorithm as an example, the onset of microseismicity could have been predicted with a 14 min warning with 99% confidence from the six sensors at this single site.

Clearly, more sophisticated detection algorithms can be envisaged that include both cumulative tilt, tilt rate changes, and strainmeters and tiltmeters data from other locations. In the example considered the dilatometer signal-to-noise ratio was a factor of 3 worse for the event partly due to their increased distances from the deflating source.

7. Conclusions

Calculations show that normal faulting in the Campi Flegrei region in March 2010 was induced by rapid transient deflation on all or part of a previously known, slowly inflating offshore magma source. The rate of deflation during the 40 min deflation event averaged a factor of 500 faster than the mean inflation rate before and after the event, suggesting that stressing rates were crucial to the inducement of seismicity. Although microseismicity occurred ≈20 min after the initiation of deflation, the mechanism for the delay is uncertain. It is possible that poroelasticity delayed the transmission of stress, but it is also possible that rupture responded either to the attainment of a static strain threshold, or it may also responded to the maximum strain rate change.

We demonstrate for the first time in the Campi Flegrei region the value of high-resolution continuous monitoring of subsurface deformation. Our analyses show that nanostrain and nanoradian sensitivities permit the cause and effect relationship between magmatic inflation/deflation and seismicity to be distinguished, with a precision not possible with InSAR or cGPS methods. We also demonstrate that the deformation signal preceded seismicity by 20 min, and at a single site exceeded 3 sigma 17 min before seismicity, and was a factor of 6 above RMS noise levels 14 min before the onset of normal faulting, providing the possibility of alerting local populations to approaching shaking. Although these findings provide grounds for optimism that future studies may provide precursors to magmatic and seismic activity in this and other areas where volcano-tectonic seismicity occurs, we caution that our results are based on a single event and a minimal spatial sampling of sensors. Additional sensors would considerably enhance our ability to identify anomalous transient deformation in the caldera were the mechanism we describe considered the basis for a potential early warning system.

Our study reveals the critical role played by transient stress reduction in inducing fault slip. This transient stress reduction occurred amid a setting of overall slow stress increase common to many tectonic systems. Our results thus have implications for the occurrence of triggered seismic slip on complex fault systems, shed light on the link between deformation and seismicity also in other volcanoes, and highlight the importance of continuous high-sensitivity deformation monitoring for hazards.

Acknowledgments

This work made use of GMT and Octave software. We are grateful to M. La Rocca for providing the two focal mechanisms used in this work. This research benefited from funding provided by European Commission's 7th Framework Programme (MED-SUV project, grant agreement N.308665) and the Italian Presidenza del Consiglio dei Ministri-Dipartimento della Protezione Civile (DPC). Scientific papers funded by the DPC do not represent its official opinions and policies. The dilatometer project belongs to Centro Regionale di Competenza AMRA and is supported by POR funds, Regione Campania. The long-baseline tiltmeters project is supported by the University of Salerno. Thanks are also due to the many technicians of INGV-Osservatorio Vesuviano and Carnegie Institution of Washington-DTM, helping in the field project and in the data transmission system. B. Di Lieto and P. Romano also helped in the project. The data used to produce the results of this paper are available on request (RS).

References

AGIP (1987), Modello geotermico del sistema flegreo (Sintesi), Technical Report, SERGMESG, San Donato, Italy.

Agnew, D. C. (2013), SPOTL: Some Programs for Ocean-Tide Loading, SIO Technical Report, Scripps Institution of Oceanography, San Diego, Calif. [Available at http://igppweb.ucsd.edu/agnew/Spotl/spotlman.pdf.]

Amoruso, A., and L. Crescentini (2009), Shape and volume change of pressurized ellipsoidal cavities from deformation and seismic data, *J. Geophys. Res.*, *114*, B02210, doi:10.1029/2008JB005946.

Amoruso, A., and L. Crescentini (2011), Modelling deformation due to a pressurized ellipsoidal cavity, with reference to the Campi Flegrei caldera, Italy, *Geophys. Res. Lett.*, *38*, L01303, doi:10.1029/2010GL046030.

Amoruso, A., L. Crescentini, and R. Scarpa (2000), Removing tidal and atmospheric effects from Earth deformation measurements, *Geophys. J. Int.*, *140*, 493–499, doi:10.1046/j.1365-246X.2000.00052.x.

Amoruso, A., L. Crescentini, A. T. Linde, I. S. Sacks, R. Scarpa, and P. Romano (2007), A horizontal crack in a layered structure satisfies deformation for the 2004–2006 uplift of Campi Flegrei, *Geophys. Res. Lett.*, *34*, L22313, doi:10.1029/ 2007GL031644.

Amoruso, A., L. Crescentini, and G. Berrino (2008), Simultaneous inversion of deformation and gravity changes in a horizontally layered half-space: Evidences for magma intrusion during the 1982–1984 unrest at Campi Flegrei caldera (Italy), *Earth Planet. Sci. Lett.*, *272*, 181–188, doi:10.1016/j.epsl.2008.04.040.

Amoruso, A., L. Crescentini, and I. Sabbetta (2014a), Paired deformation sources of the Campi Flegrei caldera (Italy) required by recent (1980–2010) deformation history, *J. Geophys. Res. Solid Earth*, *119*, 858–879, doi:10.1002/2013JB010392.

Amoruso, A., L. Crescentini, I. Sabbetta, P. De Martino, F. Obrizzo, and U. Tammaro (2014b), Clues to the cause of the 2011–2013 Campi Flegrei caldera unrest, Italy, from continuous GPS data, *Geophys. Res. Lett.*, *41*, 3081–3088, doi:10.1002/2014GL059539.

Battaglia, M., C. Troise, F. Obrizzo, F. Pingue, and G. De Natale (2006), Evidence for fluid migration as the source of deformation at Campi Flegrei Caldera (Italy), *Geophys. Res. Lett.*, *33*, L01307, doi:10.1029/2005GL024904.

Berrino, G., G. Corrado, G. Luongo, and B. Toro (1984), Ground deformation and gravity changes accompanying the 1982 Pozzuoli uplift, *Bull. Volcanol.*, *47*, 187–200.

Capuano, P., G. Russo, L. Civetta, G. Orsi, M. D'Antonio, and R. Moretti (2013), The active portion of the Campi Flegrei caldera structure imaged by 3-D inversion of gravity data, *Geochem. Geophys. Geosyst.*, *14*, 4681–4697, doi:10.1002/ggge.20276.

Chiarabba, C., M. Moretti, and P. De Gori (2006), The Vp and Vp/Vs structure of the Campi Flegrei caldera, in *Geophysical Exploration of the Campi Flegrei (Southern Italy) Caldera Interiors: Data, Methods and Results*, edited by A. Zollo et al., pp. 34–37, GNV-Officine Grafiche Francesco Giannini & Figli S.p.A., Napoli.

D'Auria, L., B. Massa, E. Cristiano, C. Del Gaudio, F. Giudicepietro, G. Ricciardi, and C. Ricco (2014), Retrieving the stress field within the Campi Flegrei caldera (southern Italy) through an integrated geodetical and seismological approach, *Pure Appl. Geophys.*, doi:10.1007/s00024-014-1004-7.

De Natale, G., A. Zollo, A. Ferraro, and J. Virieux (1995), Accurate fault mechanism determinations for a 1984 earthquake swarm at Campi Flegrei caldera (Italy) during an unrest episode: Implications for volcanological research, *J. Geophys. Res.*, *100*(B12), 24,167–24,185.

De Natale, G., S. M. Petrazzuoli, and F. Pingue (1997), The effect of collapse structures on ground deformations in calderas, *Geophys. Res. Lett.*, *24*, 1555–1558, doi:10.1029/97GL01600.

De Siena, L., E. Del Pezzo, and F. Bianco (2010), Seismic attenuation imaging of Campi Flegrei: Evidence of gas reservoirs, hydrothermal basins, and feeding systems, *J. Geophys. Res.*, *115*, B09312, doi:10.1029/2009JB006938.

Folch, A., and J. Gottsmann (2006), Faults and ground uplift at active calderas, in *Mechanisms of Activity and Unrest at Large Calderas*, edited by C. Troise, G. De Natale, and C. R. J. Kilburn, *Geol. Soc. London, Spec. Publ.*, *269*, 109–120, .

Fournier, N., and L. Chardot (2012), Understanding volcano hydrothermal unrest from geodetic observations: Insights from numerical modeling and application to White Island volcano, New Zealand, *J. Geophys. Res.*, *117*, B11208, doi:10.1029/2012JB009469.

Gaeta, F. S., F. Peluso, I. Arienzo, D. Castagnolo, G. De Natale, G. Milano, C. Albanese, and D. G. Mita (2003), A physical appraisal of a new aspect of bradyseism: The miniuplifts, *J. Geophys. Res.*, *108*(B8), 2363, doi:10.1029/2002JB001913.

Harris, A. R. (1998), Introduction to special section: Stress triggers, stress shadows, and implications for seismic hazard, *J. Geophys. Res.*, *103*, 24,347–24,358.

Judenherc, S., and A. Zollo (2004), The Bay of Naples (southern Italy): Constraints on the volcanic structures inferred from a dense seismic survey, *J. Geophys. Res.*, *109*, B10312, doi:10.1029/2003JB002876.

Lee, W. H. K., and J. C. Lahr (1975), *HYPO71 (Revised): A Computer Program for Determining Hypocenter, Magnitude and First Motion Pattern of Local Earthquakes*, *U. S. Geol. Surv.Open File Rep., 75-311*, Menlo Park, Calif.

Ludwig, W. J., J. E. Nafe, and C. L. Drake (1970), Seismic refraction, in *The Sea*, vol. 4, edited by A. E. Maxwell, pp. 53–84, Wiley-Interscience, New York.

Manconi, A., T. R. Walter, M. Manzo, G. Zeni, P. Tizzani, E. Sansosti, and R. Lanari (2010), On the effects of 3-D mechanical heterogeneities at Campi Flegrei caldera, southern Italy, *J. Geophys. Res.*, *115*, B08405, doi:10.1029/2009JB007099.

Milia, A., E. Turco, P. P. Pierantoni, and A. Schettino (2009), Four-dimensional tectono-stratigraphic evolution of the southeastern peri-Tyrrhenian basins (Margin of Calabria, Italy), *Tectonophysics*, *476*, 41–56.

McNutt, S. R. (2005), Volcanic Seismology, *Annu. Rev. Earth Planet. Sci.*, *32*, 15.1–15.31, doi:10.1146/annurev.earth.33.092203.122459.

Morhange, C., N. Marriner, J. Laborel, M. Todesco, and C. Oberlin (2006), Rapid sea-level movements and noneruptive crustal deformations in the Phlegrean Fields caldera, Italy, *Geology*, *34*, 93–96.

Orsi, G., M. A. Di Vito, and R. Isaia (2004), Volcanic hazard assessment at the restless Campi Flegrei caldera, *Bull. Volcanol.*, *66*, 514–530.

Petrosino, S., L. De Siena, and E. Del Pezzo (2008), Recalibration of the magnitude scales at Campi Flegrei, Italy, on the basis of measured path and site and transfer functions, *Bull. Seismol. Soc. Am.*, *98*, 1964–1974, doi:10.1785/0120070131.

Rosi, M., and A. Sbrana (Eds.) (1987), *Phlegrean Fields*, pp. 175, vol. 9, Quaderni de "La Ricerca Scientifica", CNR, Roma, Italy.

Saccorotti, G., S. Petrosino, F. Bianco, M. Castellano, D. Galluzzo, M. La Rocca, E. Del Pezzo, L. Zaccarelli, and P. Cusano (2007), Seismicity associated with the 2004–2006 renewed ground uplift at Campi Flegrei caldera, Italy, *Phys. Earth Planet. Inter.*, *165*, 14–24, doi:10.1016/j.pepi.2007.07.006.

Toda, S., R. S. Stein, and T. Sagiya (2002), Evidence from the AD 2000 Izu islands earthquake swarm that stressing rate governs seismicity, *Nature*, *419*, 58–61, doi:10.1038/nature00997.

Todesco, M., A. P. Rinaldi, and M. Bonafede (2010), Modeling of unrest signals in heterogeneous hydrothermal systems, *J. Geophys. Res.*, *115*, B09213, doi:10.1029/2010JB007474.

Trasatti, E., M. Polcari, M. Bonafede, and S. Stramondo (2015), Geodetic constraints to the source mechanism of the 2011–2013 unrest at Campi Flegrei (Italy) caldera, *Geophys. Res. Lett.*, *42*, 3847–3854, doi:10.1002/2015GL063621.

Troiano, A., M. G. Di Giuseppe, Z. Petrillo, C. Troise, and G. De Natale (2011), Ground deformation at calderas driven by fluid injection: Modelling unrest episodes at Campi Flegrei (Italy), *Geophys. J. Int.*, *187*, 833–847, doi:10.1111/j.1365-246X.2011.05149.x.

Venedikov, A. P., J. Arnoso, and R. Vieira (2005), New version of program VAV for tidal data processing, *Comput. Geosci.*, *31*, 667–669, doi:10.1016/j.cageo.2004.12.001.

Wang, R., F. Lorenzo-Martín, and F. Roth (2006), PSGRN/PSCMP—A new code for calculating co- and post-seismic deformation, geoid and gravity changes based on the viscoelastic-gravitational dislocation theory, *Comput. Geosci.*, *32*, 527–541, doi:10.1016/j.cageo.2005.08.006.

Zollo, A., N. Maercklin, M. Vassallo, D. Dello Iacono, J. Virieux, and P. Gasparini (2008), Seismic reflections reveal a massive melt layer feeding Campi Flegrei caldera, *Geophys. Res. Lett.*, *35*, L12306, doi:10.1029/2008GL034242.